Catalysis Science & Technology

ROYAL SOCIETY OF CHEMISTRY

PAPER

Cite this: *Catal. Sci. Technol.*, 2021, **11**, 1430

Catalytic enrichment of plasma with hydroxyl radicals in the aqueous phase at room temperature†

Maïté Audemar,[a] Oriol Vallcorba,[b] Inma Peral,[c] Jean-Sébastien Thomann,[d] Agata Przekora,[e] Joanna Pawlat,[f] Cristina Canal,[ghi] Grazyna Ginalska,[e] Michał Kwiatkowski,[f] David Duday[d] and Sophie Hermans *[a]

Received 3rd August 2020,
Accepted 3rd December 2020

DOI: 10.1039/d0cy01557a

rsc.li/catalysis

Different iron oxide catalysts supported on mesoporous silica were prepared by several techniques including assembly of pre-synthesized nanoparticles, coprecipitation in the presence of the support or impregnation. Characterization showed that iron oxide nanoparticles were dispersed either at the surface of the SiO_2 material or within the pores when prepared by dry impregnation. The catalytic performance of these materials for Fenton chemistry was evaluated through kinetic tests in the presence of coumarin as a radical trap for the quantification of the HO• radicals produced. The first tests concerned the production of HO• radicals from H_2O_2 by a Fenton-like reaction. The results show that catalysts prepared by dry impregnation in an ethanolic solution show the highest activity toward the production of HO• radicals. These catalysts were also engaged in a reaction without external H_2O_2 using a cold atmospheric pressure plasma jet treatment with the successful purpose of increasing the production of HO• radicals in aqueous solution at room temperature and near-neutral pH. Our best catalysts outperformed others reported in the literature in reactions carried out with soluble species or at acidic pH. Moreover, a synergetic effect between the heterogeneous catalyst and the plasma for HO• radical production was highlighted. These radicals could be easily used for biomedical or wastewater treatment applications.

Introduction

Advanced oxidation processes (AOPs) allow the production of highly reactive oxygen species, above all the hydroxyl (HO•) radical, which is a strong oxidant capable of oxidizing persistent organic pollutants for wastewater treatment.[1–3]

These HO• radicals can be formed by using the homogeneous Fenton reaction that implies the activation of H_2O_2 by ferrous ions (Fe^{2+}).[4,5] However, to avoid formation of soluble metallic species, serious attention has been focused on the heterogeneous Fenton-like reaction.[6] The Fenton-like reaction is based on the use of noble metals or metal oxides (Au, or Cu, Co, Mn and Fe oxide)[7,8] but the use of materials containing iron (Fe zeolites or modified clays) has also been reported.[9,10] Among all these reported catalysts, iron oxides[11] received the most interest due to their properties (magnetic properties, good activity, recyclability).[12,13]

The possibility to support these iron oxide nanoparticles on (porous or nonporous) solids can result in better dispersion and hence smaller Fe_3O_4 nanoparticles with improvement of the catalytic activity due to a larger surface area.[11,14,15] Some studies also suggest that this better activity is due to electron transfers between iron and a coating[16] or the support.[17]

[a] *IMCN Institute, Universite Catholique de Louvain, Place Louis Pasteur 1, 1348 Louvain-la-Neuve, Belgium. E-mail: sophie.hermans@uclouvain.be*
[b] *ALBA Synchrotron Light Source, Carrer de la Llum 2-26, 08290 Cerdanyola del Valles, Barcelona, Spain*
[c] *Physics and Materials Science Research Unit, Maison du Savoir, Université du Luxembourg, Avenue de l'Université 2, L-4365 Esch-sur-Alzette, Luxembourg*
[d] *Material Research and Technology (MRT) Department, Luxembourg Institute of Science and Technology (LIST), 41 rue du Brill, L-4422 Belvaux, Luxembourg*
[e] *Chair and Department of Biochemistry and Biotechnology, Medical University of Lublin, Chodzki 1 Street, 20-093 Lublin, Poland*
[f] *Chair of Electrical Engineering and Electrotechnologies, Lublin University of Technology, Nadbystrzycka 38a, 20-618 Lublin, Poland*
[g] *Biomaterials, Biomechanics and Tissue Engineering Group, Department of Materials Science and Engineering, Universitat Politècnica de Catalunya (UPC), Av. Eduard Maristany 14, 08930 Barcelona, Spain*
[h] *Barcelona Research Center in Multiscale Science and Engineering, UPC, Barcelona, Spain*
[i] *Research Centre for Biomedical Engineering (CREB), UPC, Barcelona, Spain*

† Electronic supplementary information (ESI) available: Characterization data of the different catalysts; N_2 physisorption curves of both silica supports; TEM image of the synthesized Fe_3O_4 nanoparticles with their size distribution diagram. Additionally, TPR and XRD analyses and SEM-EDX mapping for the catalysts with the highest catalytic activity (Fe_xO_y/MCM-48(I-EtOH) and Fe_xO_y/MSNPs(I)); catalytic performance of the hydrophilic Fe_3O_4 nanoparticles and demonstration of the synergetic effect between Fe_xO_y/MSNPs(I-EtOH) and plasma. See DOI: 10.1039/d0cy01557a

In the heterogeneous Fenton process, the HO$^{\bullet}$ radical can be generated by the reaction of hydrogen peroxide (H_2O_2) and the surface Fe^{II} (denoted as $\equiv Fe^{II}$) (eqn (1)). Magnetite (Fe_3O_4) indeed is a mixed Fe^{II} + Fe^{III} oxide. This simplified mechanism proposed by Lin et Gurol[18] based on surface complexation chemistry is widely accepted.[19]

$$\equiv Fe^{II} + H_2O_2 \rightarrow \equiv Fe^{III}\text{–}OH + HO^{\bullet} \quad (1)$$

The $\equiv Fe^{III}$–OH formed can also react with H_2O_2 (according to eqn (2)) to give $HO_2^{\bullet}$, allowing regeneration of Fe^{II}. This hydroperoxyl radical ($HO_2^{\bullet}$) can also be formed by the reaction between H_2O_2 and HO$^{\bullet}$ (eqn (3)) and they can participate in the regeneration of Fe^{II} according to (eqn (4)).

$$\equiv Fe^{III}\text{–}OH + H_2O_2 \rightarrow \equiv Fe^{II} + H_2O + HO_2^{\bullet} \quad (2)$$

$$HO^{\bullet} + H_2O_2 \rightarrow HO_2^{\bullet} + H_2O \quad (3)$$

$$\equiv Fe^{III}\text{–}OH + HO_2^{\bullet} \rightarrow \equiv Fe^{II} + H_2O + O_2 \quad (4)$$

The superoxide anion ($O_2^{\bullet -}$) can also be detected during the Fenton process and arises from the presence of $HO_2^{\bullet}$ (eqn (5)).

$$HO_2^{\bullet} \leftrightarrow H^+ + O_2^{\bullet -} \quad (5)$$

In the medical field, the use of HO$^{\bullet}$ radicals is studied due to its strong oxidizing power that can cause damage to DNA, cellular proteins and lipids. Studies were therefore conducted for the treatment of cancer by generation of HO$^{\bullet}$ radicals from the endogenous H_2O_2 of the tumor cells[20] or that have been brought into the tumor environment by enzymatic catalysis[21] or plasma.[22] This latter possibility stems from the recent development of atmospheric plasma. Plasma is an ionized gas containing molecules (or neutral gas atoms), electrons and different types of ions as well as excited species and radicals. Non-thermal plasma ("cold plasma") operating at atmospheric pressure has applications in analytical chemistry, plasma-catalysis,[23–25] deposition or surface modification,[26,27] biomedicine (wound healing,[28] disinfection/anti-bacterial,[29] cancer treatment[30,31]) or in depollution (water[32] or air[23]). It is well established that plasma allows the production of reactive species within the plasma[33] or upon interaction with species present in its surrounding atmosphere (such as N_2, O_2 or water vapor).[33,34] Among these reactive species, reactive oxygen and nitrogen species (RONS), in particular HO$^{\bullet}$ radicals and H_2O_2, play a key role, although many others are present and the reactivity of plasma in liquids is very complex, as shown here.[35,36] HO$^{\bullet}$ species are produced in the plasma gas phase by electron impact dissociation of H_2O during the interaction of plasma with the humidity in the air diffusing into the jet[33,34,37] or in the aqueous medium.[35]

Therefore, our goal is to combine an iron oxide catalyst with plasma excitation to generate an enhanced fraction of HO$^{\bullet}$ radicals. These radicals could be applied to water remediation or medical fields, but as a proof of principle, here they will be simply trapped to confirm their presence and obtain an evaluation of their quantity. We have chosen the known reaction of coumarin[38–40] that upon HO$^{\bullet}$ radical addition gives a fluorescent molecule: umbelliferone (Fig. 1).

Fenton chemistry is usually carried out under acidic conditions.[41,42] Our goal here is to efficiently produce HO$^{\bullet}$ radicals in pure water without pH control, at room temperature, using iron oxide supported on silica material catalysts, in a non-assisted heterogeneous Fenton reaction mode. Indeed, performant catalysts reported to date for this reaction are assisted by UV radiation.[43,44] In addition, literature reports focused on the degradation/oxidation of organic pollutants under these conditions, without any effort to isolate the active species or quantify the radicals involved. Other oxidizing agents can be involved during Fenton-like reactions. This has been highlighted indirectly by using radical scavengers that cause a lowering of the catalytic activity.[14,43] Hence the present contribution will focus on HO$^{\bullet}$ radical formation and detection without immediate further use to avoid hiding subtle effects.

Different materials will be compared for their catalytic efficiency. In this work, iron oxide nanoparticles supported over mesoporous silica have been prepared by various techniques involving either dispersion of preformed magnetite nanoparticles or impregnation of an iron salt, with the aim to obtain small iron oxide nanoparticles well dispersed on the silica support to give a "high active surface. The as-prepared materials were characterized and evaluated for the production of hydroxyl radicals in water at room temperature and atmospheric pressure. They were tested first for the heterogeneous Fenton-like process in the presence of H_2O_2 without an external light source, and second under the effect of cold atmospheric plasma treatment. The efficiency of hydroxyl radical production by combining Fenton supported nanocatalysts and cold atmospheric plasma is discussed.

Experimental

Reagents and materials

Hexadecyltrimethylammonium bromide (CTAB, 95%), tetraethyl orthosilicate (TEOS, >98%), $FeCl_3{\cdot}6H_2O$ (99+%) and $FeCl_2{\cdot}4H_2O$ (99+%) were purchased from Sigma Aldrich and used as received. 2-Bromo-2-methylpropionic acid (BMPA, 98%), 3-aminopropyltriethoxysilane (APTES, 98%) and $Fe(NO_3)_3{\cdot}9H_2O$ were purchased from Alfa Aesar, aqueous

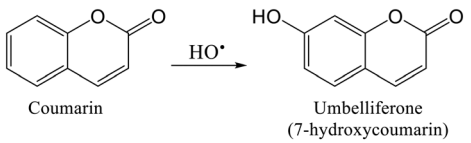

Fig. 1 Formation of the fluorescent 7-hydroxycoumarin by the reaction of HO$^{\bullet}$ radicals with coumarin.

ammonia (28–30 wt%) from ChemLab and coumarin (99+%), H_2O_2 (35 wt%) and oleic acid (80–90%) from Acros Organics. Citric acid (p.a.) was purchased from Merck. A commercial ultrasonic cleaner (VWR) was used for sonication.

Syntheses of iron oxide-based catalysts

Silica supports. Spherical MCM-48 mesoporous silica particles were synthesized according to a procedure reported by Schumacher and co-workers.[45] The template *n*-hexadecyltrimethylammonium bromide (CTAB, 2.4 g) was dissolved under stirring in a mixture of deionized water/ethanol (50 mL/50 mL) at room temperature followed by the addition of aqueous ammonia (28–30 wt%, 12 mL) and this solution was left under stirring for 10 min. Then, the silica source tetraethyl orthosilicate (TEOS, 3.4 g; 16 mmol) was added and the mixture was stirred still at room temperature for 2 h under constant stirring. The molar ratio of this reaction is TEOS/CTAB/NH_3/H_2O/EtOH 1/0.4/12.5/174/54. The resulting solid was filtered out, washed with distilled water and dried in air at room temperature. The MCM-48 support was obtained by calcination under air at 550 °C for 6 h to remove the CTAB template.

Wormhole and interconnected pore mesoporous silica nanoparticles (MSNPs) were synthesized using surfactant-directed, base-catalyzed condensation of silica precursors using a sol–gel approach proposed earlier by Bein and co-workers.[46] A stock solution was prepared by mixing 13.75 mL of Milli-Q water, 2.23 mL of absolute ethanol, and 2.23 mL (1.69 mmol) of cetyltrimethylammonium chloride (CTACl, 25 wt%) by stirring in a Radleys Mya 4® station for 10 min under an argon atmosphere. Then, triethanolamine (TEA, 1.78 mL; 13.37 mmol) was added to the stock solution and mixed at room temperature until complete dissolution. When TEA was fully dissolved, the mixture was heated at 60 °C, and then TEOS (1.454 mL; 6.5 mmol) was added dropwise. The reaction was further stirred for 2 h under an argon atmosphere. The molar ratio of this reaction is TEOS/CTACl/TEA/H_2O/EtOH 1/0.26/2/117.35/5.88. The solid was recovered and extraction of the CTACl surfactant was achieved by applying several cycles of hydrochloric acid wash/centrifugation. Each extraction cycle included a dispersion of MSNPs in a solution of ethanol and hydrochloric acid at 2%, ultrasonication for 40 min at 40 °C and then centrifugation for 20 min at 45 000*g*. After surfactant extraction, MSNPs were either dispersed in absolute ethanol or freeze-dried to obtain a dried powder.

Fe_3O_4 NPs. Magnetite nanoparticles were prepared by the coprecipitation method.[47] Namely, 5.85 g of $FeCl_3{\cdot}6H_2O$ and 2.2 g of $FeCl_2{\cdot}4H_2O$ were dissolved in 200 mL of distilled water and the mixture was left under argon bubbling for 1 h. Then the solution was heated to 90 °C, 9 mL of aqueous ammonia (28–30 wt%) was added and the mixture was kept at this temperature for 20 min. To obtain hydrophobic magnetite nanoparticles, 9 mL of oleic acid was added directly to the mixture and kept under stirring for 60 min at 90 °C. After cooling, the nanoparticles were separated by using an external magnet (magnetic decantation) and washed with distilled water.

To obtain hydrophilic magnetite nanoparticles, the black precipitate was recovered with a magnet after the 20 min period at 90 °C and washed with distilled water. Then, 2 g of citric acid was added to the redispersed nanoparticles in 200 mL of distilled water and the mixture was heated to 80 °C for 30 min. After cooling, the nanoparticles were separated by magnetic decantation and washed with distilled water.

Fe_3O_4/MCM-48(CV). These magnetite NPs have been linked to the MCM-48 surface. For this, the surface of MCM-48 was first functionalized[48] with amino groups by treatment with APTES (3-aminopropyltriethoxysilane) as follows. MCM-48 (1 mg) was dispersed in 100 mL of ethanol and the mixture was refluxed for 3 h followed by the addition of 400 μL of APTES. The solid was recovered by centrifugation and washed with ethanol.

Then, the oleic acid ligands of the magnetite nanoparticles were exchanged by reacting with BMPA (2-bromo-2-methylpropionic acid) to functionalize the surface with amine groups.[49] 50 mg of hydrophobic magnetite nanoparticles capped with oleic acid dispersed in 3 mL of chloroform was added to 30 mL of a 0.1 mol L^{-1} solution of BMPA in chloroform. The solution was left under stirring at room temperature for 48 h, then the nanoparticles were precipitated by the addition of an excess of ethanol. The precipitated Fe_3O_4–Br nanoparticles were recovered by centrifugation.

The ligand-exchanged magnetite nanoparticle dispersion (0.005 g in 3 mL of THF) was added to 0.1 g of the amino-functionalized MCM-48 dispersed in 20 mL of THF, and the resulting dispersion was heated to reflux for 3 h. The sample, designated Fe_3O_4/MCM-48(CV), was recovered by centrifugation and washed with ethanol to remove excess magnetite nanoparticles.

Fe_3O_4/MCM-48(CP). Another way used to obtain magnetite NPs on the surface of the MCM-48 was adapted from a coprecipitation method for which the preparation of magnetite nanoparticles was carried out in the presence of the MCM-48 support. To do so, 70 mg of $FeCl_3{\cdot}6H_2O$ and 26 mg of $FeCl_2{\cdot}4H_2O$ were dissolved in 4 mL of distilled water and the mixture was left under argon bubbling for 1 h. Then the solution was heated to 90 °C and 0.5 mL of aqueous ammonia (28–30 wt%) was added and the mixture was kept at this temperature for 20 min. After cooling, the nanoparticles were separated by using an external magnet (magnetic decantation) and washed with distilled water.

Fe_3O_4/MCM-48(FI). Magnetite nanoparticles were also dispersed on the MCM-48 support by impregnation assisted by ultrasound. To do so, 15 mg of hydrophilic magnetite nanoparticles were dispersed in 3 mL of deionized water before addition of 285 mg of MCM-48 particles and the mixture was left under ultrasonic irradiation for 60 min. Then, the mixture was dried under vacuum at 40 °C. The same procedure was applied to hydrophobic magnetite nanoparticles that were dispersed in chloroform.

Fe_xO_y/SiO_2(I). Finally, a dry impregnation method has also been implemented to obtain iron oxide dispersed on MSNPs. The silica support (0.3 g) was impregnated with 0.3 mL of an aqueous (or ethanolic) solution of $Fe(NO_3)_3{\cdot}9H_2O$; the concentration of the solution was adjusted to obtain a metal loading of 5 wt%. The impregnated powder was dried at 100 °C for 12 h in stagnant air and was then calcined at 500 °C in a muffle oven. The iron oxide catalyst was reduced just before the catalytic tests at the desired temperature under a reductive gas flow (Alphagaz™ mix H_2 5%/Ar, Air Liquide).

Table 1 summarizes the various preparation methods used to produce the different materials described in this study and their corresponding code names.

Characterization

The powders were characterized by transmission electron microscopy (TEM), powder X-ray diffraction (XRD), synchrotron XRD, X-ray photoelectron spectroscopy (XPS), N_2 physisorption, elemental analyses (ICP), thermogravimetric analysis (TGA) and temperature-programmed reduction (TPR).

The morphology of the samples was evaluated by transmission electron microscopy (TEM). Images were obtained on a LEO 922 Omega energy filter transmission electron microscope operating at 120 kV. The samples were suspended in acetone under ultrasonic treatment. A drop of the suspension was deposited on a holey carbon film supported on a copper grid (Holey Carbon Film 300 Mesh Cu, Electron Microscopy Sciences), which was dried overnight under vacuum at room temperature before introduction in the microscope.

SEM and SEM-EDX (energy-dispersive X-ray spectrometry) analyses were performed using a JEOL FEG SEM 7600F equipped with an EDX system (Jeol JSM2300 with a resolution <129 eV) operating at 15 keV with a working distance of about 8 mm. The acquisition time for the chemical spectra lasted 300 s with a probe current of 1 nA. The quantitative analysis of the atomic elements was performed using the integrated Analysis Station software. A two-step analysis procedure was applied in order to obtain quantitatively reliable results for the element profiles over the entire cross sections: (i) the subtraction of the bremsstrahlung done with the classical top-hat filter method[50,51] and (ii) the quantification of the area under each atomic peak determined by the $\varphi(\rho z)$ model.[52–54]

Synchrotron X-ray powder diffraction measurements were performed at the MSPD beamline of the ALBA synchrotron.[55] The samples were inserted into 0.7 mm glass capillaries and diffraction data were collected at 30 keV (0.41335 Å wavelength) in transmission mode using the MYTHEN detector (6 molecules at 550 mm from the sample) up to 120° (2θ) and a total measurement time of 30 min per sample.

X-ray photoelectron spectroscopy (XPS) analyses were carried out at room temperature using an SSI-Xprobe (SSX 100/206) photoelectron spectrometer from Surface Science Instruments (USA) equipped with a monochromatized microfocus Al X-ray source. Samples were stuck onto small sample holders using double-face adhesive tape and then placed on an insulating Macor® ceramic carousel. Charge effects were avoided by placing a nickel grid above the samples and using a flood gun set at 8 eV. The binding energies were calculated with respect to the C–(C, H)

Table 1 Summary of preparation methods tested and corresponding code names for the obtained materials

Preparation method	Code name
MCM-48 support	MCM-48
Mesoporous silica nanoparticle support	MSNPs
Hydrophobic magnetite NPs obtained from the coprecipitation of Fe(II)/Fe(III) salts and coated with oleic acid	Fe_3O_4(o)
Bromo-terminated magnetite nanoparticles (after ligand exchange of Fe_3O_4(o))	Fe_3O_4–Br
Hydrophilic magnetite NPs obtained from the coprecipitation of Fe(II)/Fe(III) salts and coated with citric acid	Fe_3O_4(i)
Surface-modified Fe_3O_4 NPs covalently linked on the surfaced-modified MCM-48	Fe_3O_4/MCM-48(CV)
Ferrofluid impregnation: Fe_3O_4(o) NPs dispersed in $CHCl_3$	Fe_3O_4(o)/MCM-48(FI)
Ferrofluid impregnation: Fe_3O_4(i) NPs dispersed in H_2O	Fe_3O_4(i)/MCM-48(FI)
Coprecipitation of Fe(II)/Fe(III) salts in the presence of MCM-48	Fe_3O_4/MCM-48(CP)
Dry impregnation (with aqueous solution) onto MCM-48 and thermal activation at the indicated temperature	Fe_xO_y/MCM-48(I) (*XXX*°)
Dry impregnation (with ethanolic solution) onto MCM-48	Fe_xO_y/MCM-48(I-EtOH) (500°)
Dry impregnation (in EtOH) onto MSNPs	Fe_xO_y/MSNPs(I-EtOH) (500°)

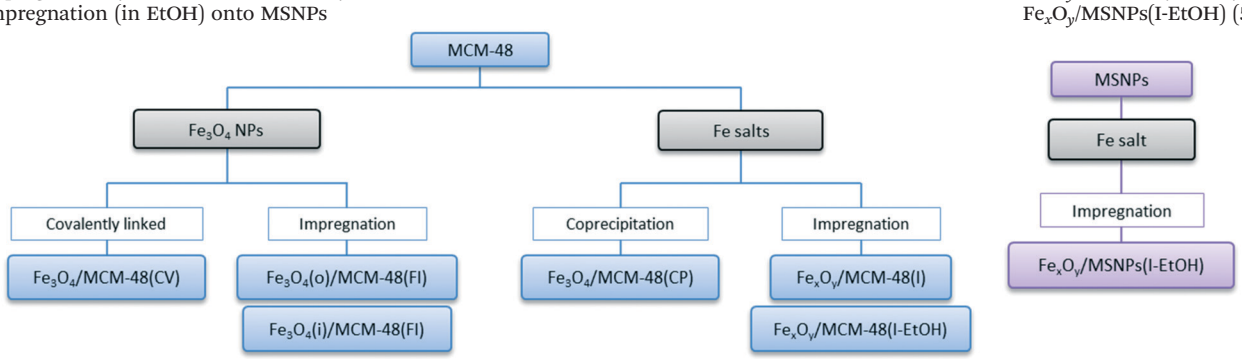

component of the C1s peak fixed at 284.8 eV. Data treatment was performed using the CasaXPS program (Casa Software Ltd., UK). The peaks were decomposed into a sum of Gaussian/Lorentzian (85/15) after subtraction of a Shirley-type baseline.

The pore texture of the covered catalysts was characterized by nitrogen adsorption–desorption isotherms. The measurements were achieved by using a Micromeritics ASAP 2020 analyzer at 77 K. Before analysis, the samples (0.02–0.10 g) were degassed for 2 h at 200 °C at a heating rate of 10 °C min^{-1} under 0.133 Pa pressure. The analysis of the isotherms provided specific surface areas calculated with the Brunauer–Emmett–Teller (BET) equation, S_{BET}. The pore volume, V_p, of the samples and the pore average diameter were calculated using the DFT model.

Iron and gold were analyzed by ICP-AES on an ICAP 6500 instrument. The samples were prepared by an acid digestion process.

Powder X-ray diffraction (XRD) was performed on a Bruker D8 advanced diffractometer with Bragg Brentano geometry, using a LinkEye XE-T detector with Cu Kα radiation (λ = 0.154 nm) and a power of 1200 W (40 kV, 30 mA). The samples were scanned from 0.8 to 10 (2θ range) at a scanning rate of 1.5° min^{-1}.

Thermograms were recorded on a TGA/SDTA 851e instrument from Mettler Toledo. Samples (5–10 mg) in alumina containers were heated at 10 °C min^{-1} under air flow.

Temperature-programmed reduction (TPR) with hydrogen was used to evaluate the reduction temperature of the iron-based catalyst. A Hiden Catlab Reactor combined with a QGA Hiden Quadrupole mass spectrometer was used. The sample was pretreated in dry air (20 mL min^{-1}) at 500 °C for 1 h. The sample was then cooled under argon (20 mL min^{-1}) to 120 °C. After 1 h under argon flow, the gas flow was changed to a mixture of 15 mL min^{-1} of argon and 5 mL min^{-1} of 5% H_2 in nitrogen. A temperature program of 10 °C min^{-1} up to 650 °C was then applied.

Catalytic tests

In a typical experiment for the production of HO$^{\bullet}$ radicals, 10 mg of catalyst were added to 20 mL of a solution of 1.0 mmol L^{-1} coumarin and 9.6 × 10^{-2} mmol L^{-1} H_2O_2 in a quartz round-bottom flask equipped with a magnetic stirrer. When specified, the solution was acidified by adding a few drops of diluted HCl. At regular and defined time intervals (t = 0 min when the catalyst was added), aliquots of the solution were taken and placed in a 5 × 5 mm cell, and the fluorescence spectrum of the generated 7-hydroxycoumarin was measured after a dilution by 4 (excitation wavelength: 346 nm; emission wavelength: 452 nm) on a Cary Eclipse fluorescence spectrophotometer (from Agilent).

Catalytic tests were also carried out under plasma treatment without an external source of H_2O_2. Indeed, plasma generates H_2O_2 spontaneously on contact with water through dissociation of water molecules by reactive plasma species. For this, an atmospheric plasma jet device was used as follows. A hand-held mobile kINPen®11 plasma generator (CE-certified medical device) was operated with a power supply unit and a gas supply unit.[56] The plasma jets consisted of a central pin type electrode that ignited plasma by applying a voltage of 3 kV at a frequency of approximately 1.1 MHz. Argon was used as a feed gas (5 standard liters per minute) because it is known to generate a higher content of H_2O_2 in the presence of water.[57] The typical plasma effluent length is 8–12 mm with a diameter of 1 mm. In a typical experiment for the production of HO$^{\bullet}$ radicals under plasma treatment, 10 mg of catalyst was added to 20 mL of a solution of 1.0 mmol L^{-1} coumarin in a quartz round-bottom flask equipped with a magnetic stirrer. Aliquots were analyzed as mentioned above.

Results and discussion

In this work, several iron oxide-based catalysts supported on mesoporous silica have been prepared by different approaches. The first section of this manuscript describes their synthesis and detailed characterization. In the second part of the paper, their activity toward the production of hydroxyl (HO$^{\bullet}$) radicals from H_2O_2 will be described, before testing HO$^{\bullet}$ radical production from pure water under plasma treatment.

Preparation of Fe_xO_y nanoparticles supported on MCM-48 mesoporous silica

The aim when preparing these catalysts was to obtain small iron oxide nanoparticles that are well dispersed on the silica support. To achieve this, several methods were used to form and support iron oxide nanoparticles on mesoporous silica. Thus, pre-synthesized Fe_3O_4 nanoparticles were covalently linked or simply deposited by impregnation. A deposition method by coprecipitation was also used to obtain very small Fe_3O_4 nanoparticles on the MCM-48 support. The last method envisaged is dry impregnation in order to confine the iron oxide nanoparticles in the silica pores.

First, MCM-48 mesoporous silica was prepared following the procedure of Schumacher and co-workers.[45] This support exhibited a high specific surface area of 1440 m^2 g^{-1} and an extremely narrow pore size distribution centered on an average of 2.7 nm (ESI,† Fig. S1). On this support, several techniques for the deposition of iron oxide nanoparticles were implemented.

A first approach was to synthesize free-standing magnetite nanoparticles before attaching them onto the MCM-48 support. Hydrophobic nanoparticles were prepared by a coprecipitation method with iron(II) and iron(III) salts in the presence of oleic acid as a coating agent.[47] The synthesized hydrophobic nanoparticles presented an average particle size distribution centered on 7.5 nm (ESI,† Fig. S2). Characterization by X-ray powder diffraction (XRD) showed peaks attributable to magnetite Fe_3O_4 and/or maghemite

γ-Fe_2O_3 phases, which were very difficult to distinguish because the two phases present a spinel structure and similar lattice parameters (Fig. S3†).

Aiming at assembling these Fe_3O_4 nanoparticles onto the MCM-48 surface, the capping oleic acid ligands were exchanged with 2-bromo-2-methylpropionic acid (BMPA).[49] The surface of the MCM-48 support was also modified with 3-aminopropyltriethoxysilane (APTES).[48] Then, the surface-modified nanoparticles were put in contact with the amine-grafted MCM-48 support. This reaction of the functionalized siliceous surface with the functionalized NPs leads to their strong covalent attachment.[48,49]

Transmission electron microscopy (TEM) images of this Fe_3O_4/MCM-48(CV) material in Fig. 3(a) show nanoparticles dispersed on the surface of the MCM-48 with the presence of some small aggregates, even if these particles tend to cluster easily.

Based on the properties of these hydrophobic Fe_3O_4 nanoparticles capped with oleic acid to form a ferrofluid when dispersed in chloroform, direct impregnation without functionalization was performed by adding the MCM-48 solid to the suspension under ultrasonic stirring, giving the catalyst named Fe_3O_4(o)/MCM-48(FI). Direct impregnation was also performed with an aqueous ferrofluid of hydrophilic Fe_3O_4 nanoparticles coated with citric acid,[58] giving the catalyst named Fe_3O_4(i)/MCM-48(FI).

These ferrofluid impregnation processes resulted in a better dispersion of Fe_3O_4 nanoparticles on the MCM-48 support with smaller aggregates, for both hydrophobic and hydrophilic magnetite nanoparticles (Fig. 3(b) and (c)).

XRD characterization of these materials (ESI,† Fig. S4) obtained by impregnation of Fe_3O_4 nanoparticle ferrofluids showed a weak intensity peak at 35.5° attributable to Fe_3O_4 magnetite or γ-Fe_2O_3 maghemite, the latter being due to an oxidation of the magnetite phase under ambient air.

Another synthetic approach was to synthesize the Fe_3O_4 nanoparticles by coprecipitation in the presence of the MCM-48 support (denoted Fe_3O_4/MCM-48(CP)). This method was used to prepare small Fe_3O_4 nanoparticles well dispersed on the graphene oxide support.[17] With this method, Fe_3O_4 nanoparticles were obtained on the MCM-48 surface but TEM imaging showed the formation of numerous and voluminous iron oxide nanoparticle aggregates (Fig. 4(a)). This method also impacted the MCM-48 structure (Fig. 4(a)) with a drop of the specific surface area from 1440 $m^2\ g^{-1}$ for the bare MCM-48 to 555 $m^2\ g^{-1}$ after the coprecipitation and with a much wider pore size distribution (ESI,† Fig. S5). Strikingly, most of the narrow mesopores have disappeared from the pore size distribution; larger mesopores have then appeared, pointing towards MCM restructuring during the iron phase deposition process. This is due to the basic pH during Fe_3O_4 coprecipitation.[59]

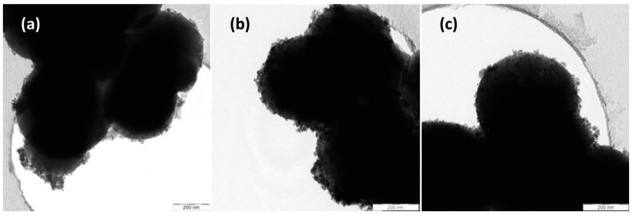

Fig. 3 TEM images of (a) magnetite/maghemite nanoparticles covalently linked to surface-modified MCM-48, (b) hydrophobic magnetite nanoparticles impregnated on MCM-48 from $CHCl_3$ suspension and (c) hydrophilic magnetite nanoparticles impregnated on MCM-48 in water.

Finally, a last kind of approach was used to obtain iron oxide NPs well dispersed on the MCM-48 support. Dry impregnation with $Fe(NO_3)_3{\cdot}9H_2O$ was performed followed by reduction under H_2 : Ar (1 : 4 V : V) after the calcination step. Two different solvents (DI water and ethanol) were compared to carry out the iron(III) nitrate impregnation into the MCM-48 support. For the Fe_xO_y/MCM-48(I) catalysts obtained with this deposition method, in either of both solvents, the iron oxide particles were not clearly visible on the TEM images (Fig. 4(b) and (c)) and X-ray diffraction (XRD) (ESI,† Fig. S6(a)) showed no signal of iron oxide phases.

Aiming at obtaining the Fe_3O_4 species and based on literature data,[60,61] a reduction step under a reductive gas flow (Alphagaz™ mix H_2 5%/Ar from Air Liquide) was performed at a temperature of 400 °C. In parallel, temperature-programmed reduction (TPR) was performed on

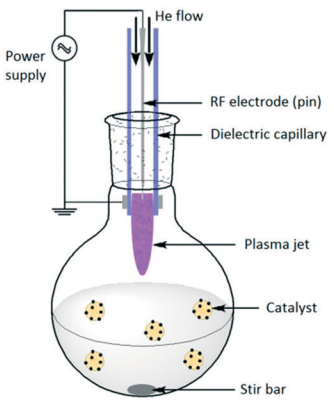

Fig. 2 Scheme of the treatment performed with cold atmospheric pressure plasma with suspensions of the catalytic particles developed. The plasma jet is not in direct contact with the suspension.

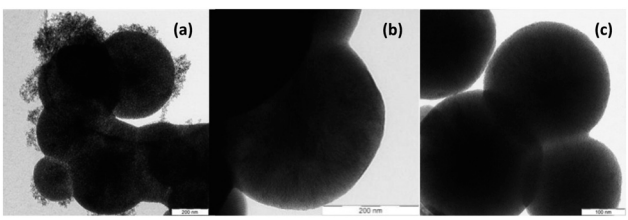

Fig. 4 TEM images of (a) magnetite nanoparticles supported on MCM-48 obtained by deposition–precipitation in the presence of the MCM-48 support (Fe_3O_4/MCM-48(CP)), (b) the Fe_xO_y/MCM-48(I-water) catalyst obtained by dry impregnation with an aqueous solution of iron(III) nitrate and (c) the Fe_xO_y/MCM-48(I-EtOH) catalyst obtained by dry impregnation with an ethanolic solution of iron(III) nitrate.

the fresh Fe_xO_y/MCM-48(I) catalyst to study the reduction profile and identify precisely the temperature of the different reduction steps (ESI,† Fig. S8). It is well known that the reduction of bulk iron oxide by hydrogen usually proceeds through the following steps: $Fe_2O_3 \rightarrow Fe_3O_4 \rightarrow FeO \rightarrow Fe$, but experimentally FeO is usually not detected.[62] In accordance with the literature, the TPR profile of our catalyst exhibits two reduction peaks. The first peak observed (~420 °C) was therefore assigned to the reduction from Fe_2O_3 to Fe_3O_4. The second peak (~575 °C) then includes two reduction steps: from Fe_3O_4 to FeO and from FeO to metallic Fe. Therefore, the temperature was varied for the reduction step carried out under a reductive gas flow (Alphagaz™ mix H_2 5%/Ar from Air Liquide) to study its influence on the catalytic properties. New samples were prepared and reduced at 500 and 600 °C.

For the catalyst prepared by dry impregnation with the aqueous solution of iron(III) nitrate (Fe_xO_y/MCM-48(I)), the iron loading was measured by ICP, which gave a value of 4.7 wt%. The surface iron content measured by XPS reached 0.50 at% (Table 2) corresponding to ~1.4 wt% (calculated). By comparing the bulk mass percentage of iron in this catalyst (ICP) with the amount of iron on the surface (XPS), it can be seen that the surface content was much lower than in the bulk. This can be explained by the iron being mainly located inside the pores of the MCM-48 support, as expected for a dry impregnation method, thanks to the low amount of solvent used that seeped into the pores by capillarity.

This observation has been confirmed by the diminution of the cumulative pore volume in the Fe_xO_y/MCM-48(I) sample as compared to the starting MCM-48 (Fig. 5), especially in the range >27 Å.

The catalysts prepared by dry impregnation or impregnation with the ferrofluid and by coprecipitation in the presence of MCM-48 were further characterized by synchrotron X-ray diffraction. Similar XRD patterns appeared, composed of large peaks arising from the mesoporous material together with, in some of the samples, clearly visible iron oxide peaks. In particular, Fe_3O_4/MCM-48(FI) presented clear Fe_3O_4 crystalline phase diffraction peaks (Fig. 6).

The most important peak of the Fe_3O_4 phase was used as a reference, and when plotting the data within this range (Fig. 6, inset), one can see that for Fe_3O_4(i)/MCM-48(FI) and Fe_3O_4/MCM-48(CP) there is some crystallinity. By integrating the area under the peak for Fe_3O_4/MCM-48(CP), we can evaluate that it corresponded to ~6% of the peak area in sample Fe_3O_4(i)/MCM-48(FI).

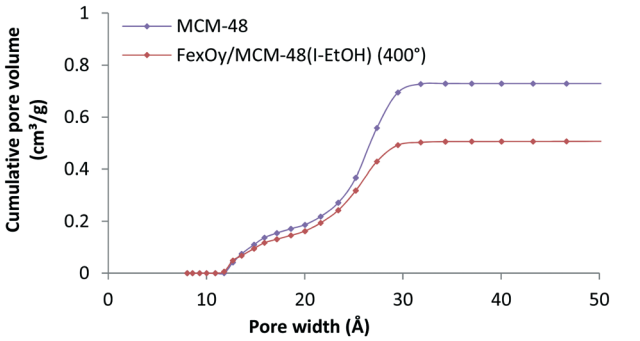

Fig. 5 Difference in cumulative pore volume before and after the dry impregnation procedure.

Using the Williamson–Hall plot to obtain the average size as well as the refinement of the whole pattern with the FullProf program, the average size of iron oxide NPs of the Fe_3O_4(i)/MCM-48(FI) sample is 10(2) nm. It is not possible to obtain a precise estimation of the size of Fe_3O_4/MCM-48(CP) either with the Williamson–Hall plot or with the Scherrer equation since there are not enough diffraction peaks in the pattern and the peak area is very small. However, the peak can be quite well reproduced if the factor 0.06 is applied to Fe_3O_4(i)/MCM-48(FI); one possible interpretation would be that about 6% of iron oxide NPs is nanocrystalline (~10 nm average size), while the rest is amorphous or smaller in size.

Fe_xO_y/MCM-48(I) does not present any indication of diffraction peaks in this region. This indicated that the particles are either amorphous or very small. Experimentally, peaks with the integrated area under 2% of the peak area for Fe_3O_4(i)/MCM-48(FI) would be undetectable, the same applies to peaks with the same area as Fe_3O_4(i)/MCM-48(FI) but with average sizes below 2 nm (please note that the width of the peak would be ~5 times larger which will hinder the peak detection). Therefore, if crystalline, the nanoparticles in Fe_xO_y/MCM-48(I) are below 2 nm in size.

Transfer of best synthesis methods from MCM-48 to mesoporous silica nanoparticles (MSNPs)

A second type of mesoporous silica (MSNP) support was prepared and characterized. This material presented much smaller particulate sizes. After efficient removal of the CTACl template, these MSNPs were characterized by N_2 physisorption: they exhibited a specific surface area of 935 $cm^2\ g^{-1}$ with an average pore diameter of 2.8 nm and a pore

Table 2 XPS results (at%) for the Fe_xO_y/MCM-48(I) and Fe_xO_y/MSNPs(I-EtOH) samples, in comparison with pure MCM-48

	MCM-48	MSNPs	Fe_xO_y/MCM-48(I)	Fe_xO_y/MCM-48(I-EtOH)	Fe_xO_y/MSNPs(I-EtOH)
O 1s	68.99	60.50	63.34	64.24	68.80
Si 2p	29.74	30.87	31.80	33.41	29.18
O/Si	2.32	1.96	1.99	1.92	2.36
Fe 2p3	—	—	0.50	0.32	0.61
Fe/Si	—	—	0.02	0.01	0.02
C 1s	1.27	8.63	4.35	2.03	1.41

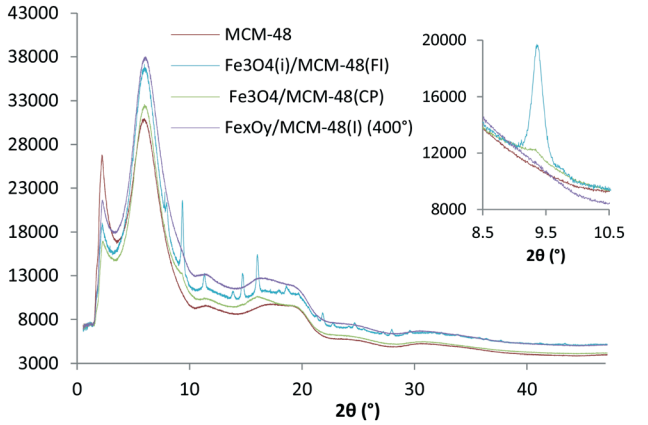

Fig. 6 Synchrotron XRD characterization of iron oxide nanoparticles supported on MCM-48 (right, zoom-in region of the Fe_3O_4 phase most intense diffraction peak).

volume of 0.61 cm^3 g^{-1} (ESI,† Fig. S9). These MSNPs had a narrow pore size distribution, which was validated by the absence of hysteresis on the type IV isotherm. The morphology of these MSNPs was observed by electron microscopy (SEM, Fig. S10, ESI†) and the images showed spherical and monodisperse particles with an average diameter of 53 ± 6 nm.

The dry impregnation procedure with an ethanolic solution of $Fe(NO_3)_3{\cdot}9H_2O$ gave the best results on MCM-48 amongst all procedures screened as described above. This optimal synthetic procedure to decorate the silica with iron oxide nanoparticles was therefore repeated with this new mesoporous silica nanosupport to give the sample named Fe_xO_y/MSNPs(I-EtOH).

XPS characterization of this material (Table 2) revealed that the iron at the surface on the silica support was only present at a loading rate of 0.61 at% corresponding to ~1.75 wt% (calculated).

XRD analysis of this catalyst showed a very small peak at 35.5° (ESI,† Fig. S6(b)) corresponding to the most intense diffraction peak of magnetite Fe_3O_4 or maghemite γ-Fe_2O_3, indicating that the iron oxide NPs in this case were at least partially crystalline or slightly bigger than with the MCM-48 support.

Again, the TEM images of this material showed no clearly visible iron oxide nanoparticles (ESI,† Fig. S11), confirming as expected their very small sizes. Finally, SEM and elemental mapping images of Fe_xO_y/MSNPs(I-EtOH) (ESI,† Fig. S11) revealed the homogeneously dispersed iron within the support particles.

Production of HO˙ radicals

As mentioned above, the activity of all of these catalysts was evaluated in a first step for the catalytic production of HO˙ radicals from H_2O_2 to compare the different materials. Then, the most active catalysts were evaluated for the catalytic production of HO˙ radicals in water without H_2O_2 but under cold atmospheric plasma treatment of the catalyst suspension. This innovative part aims at exploring possible synergetic effects between plasma and catalytic materials. In this case, the tests were carried out by treating the solution continuously with a low-temperature plasma jet supplied with chemically inert argon gas. Still, this treatment was performed in an open-batch reactor, where the liquid surface was in contact with air. In addition to reactive oxygen species, which are formed from activation and non-equilibrium dissociation of water molecules in the liquid phase, these conditions may support the formation of many types of active compounds also including molecules containing the nitrogen atom, primarily formed in the gaseous phase surrounding the plasma plume and further dissolving into the liquid phase. However, the main goal of the present investigation was to elaborate experimental conditions that with plasma-assisted catalytic activity strongly promote the generation of HO˙ radicals.

In both cases, the catalytic production of the HO˙ radicals was followed through a fluorescence method based on the reaction between the HO˙ produced and coumarin to produce 7-hydroxycoumarin, a highly fluorescent product (see Fig. 1).

The production of HO˙ radicals was first tested with the support alone and then studied in the presence of the iron-based catalysts and H_2O_2 (Fenton-like reaction) at room temperature and atmospheric pressure. The MCM-48 present during the reaction had no activity toward the production of the HO˙ radicals (not shown).

In the case of the catalyst where the surface-modified magnetic nanoparticles were prepared separately before being assembled onto the MCM-48, no activity for the production of HO˙ radicals was noticed under our conditions. Therefore, the surface-modified magnetite nanoparticles as well as the surface-modified MCM-48 (Fe_3O_4/MCM-48(CV)) have been studied by TGA under air (ESI,† Fig. S12) to assess whether it is possible to remove the capping agents to evaluate if they do not hinder the activity towards the production of HO˙ radicals. For the coated Fe_3O_4 NPs it was possible to observe a mass loss between 200 °C and 380 °C (TGA) with a wide exothermic peak in this temperature range (DSC) and a second exothermic peak without real mass change around 560 °C. The first mass loss can be attributed to the decomposition of the capping agents. A mass loss was also observed at *ca.* 300 °C for the surface-modified MCM-48 that can be attributed to the loss of the APTES functionalization, in addition to a loss before 100 °C corresponding to water physisorbed on the silica surface.

This Fe_3O_4/MCM-48(CV) catalyst was therefore thermally treated under air at 400 °C. However, after this thermal treatment aiming at eliminating organic compounds from the Fe_3O_4 NPs and MCM-48 surface, the catalyst was still inactive toward the production of HO˙ radicals from H_2O_2 under our experimental conditions. This is ascribed to a concomitant phase transition of magnetite into maghemite (as indicated by the first and wide exothermic peak), leading to all the iron being in the Fe(III) state. This inhibits the

activity toward the production of HO$^{\bullet}$ radicals from H_2O_2. In the literature, the transformation of Fe_3O_4 into γ-Fe_2O_3 (maghemite) is reported to occur at a temperature between 200 and 400 °C (ref. 63) and the second exothermic peak can be attributed to another phase transition as maghemite is transformed into the hematite phase.[64]

The catalyst prepared by impregnation of the hydrophobic Fe_3O_4 NP ferrofluid (Fe_3O_4(o)/MCM-48(FI)) did not show either any activity toward the production of HO$^{\bullet}$ radicals from H_2O_2. However, the hydrophobic character of these Fe_3O_4 NPs was not ideally suited because the reaction was carried out in water. Thus, as described above, hydrophilic Fe_3O_4 NPs were also impregnated on MCM-48 (Fe_3O_4(i)/MCM-48(FI)). The hydrophilic Fe_3O_4 NPs tested alone (unsupported) exhibited activity for HO$^{\bullet}$ radical production from H_2O_2 (ESI,† Fig. S13). However, the process of supporting them on MCM-48 led to a complete loss of activity.

The catalyst obtained by coprecipitation in the presence of the MCM-48 support (Fe_3O_4/MCM-48(CP)) was active for the production of HO$^{\bullet}$ radicals from H_2O_2 (Fig. 7, orange curve (▲)) despite the non-optimal dispersion of the nanoparticles on the MCM-48 surface (see above, Fig. 4(a)).

Production of HO$^{\bullet}$ radicals from H_2O_2 was also obtained with the catalyst prepared by dry impregnation followed by a reduction step under H_2 (Fig. 7, purple curve (■)).

This result could be explained by the size of the iron oxide nanoparticles. Indeed, the characterization results seem to show that they are slightly bigger in Fe_3O_4/MCM-48(CP) than in Fe_xO_y/MCM-48(I). Previous studies stated that the catalytic activity in the Fenton-like reaction is improved with smaller Fe_3O_4 particles which allow better dispersion and larger surface area.[11,14,15] However, it should be noted that Niu *et al.*[16] indicated that they found only a limited relationship between the improvement in catalytic activity and the size of their humic acid (HA) coated Fe_3O_4 particles. They suggested rather that this improvement could be due to the electron transfer among the complexed Fe(II)–HA or Fe(III)–HA allowing a rapid regeneration of the Fe(II) species. This hypothesis has also been proposed by Zubir *et al.*[17] due to the strong interaction between the Fe_3O_4 nanoparticles and the support in their graphene oxide–Fe_3O_4 nanocomposites.

With the iron oxide catalyst, it is known that it is the presence of iron in the Fe(II) state which is active during the Fenton-like reactions for HO$^{\bullet}$ radical production from H_2O_2.[4,5,13] Therefore, according to the TPR results presented above (ESI,† Fig. S8), the ideal reduction temperature would be in a window between the two reduction peaks at ~480 to ~540 °C. The catalytic tests carried out with additional samples reduced at 500 and 600 °C were in agreement with an improvement in the production of HO$^{\bullet}$ radicals from H_2O_2 when the catalyst was reduced at 500 °C instead of 400 °C, but increasing the reduction temperature to 600 °C led to the formation of Fe(0), causing a fall in its activity due to the lack of Fe(II) (Fig. 8).

In subsequent experiments, the reduction step for all the catalysts prepared by dry impregnation was performed just before the catalytic tests and at a temperature of 500 °C.

An increase in the activity for the production of HO$^{\bullet}$ radicals from H_2O_2 was observed when the solvent of the dry impregnation was changed to ethanol (Fig. 9). This effect is probably due to an influence of the impregnation solvent on the iron oxide particle sizes obtained. Ho *et al.*[65] and Zhang *et al.*[66] obtained smaller crystallites (and so a higher dispersion) when impregnating cobalt nitrate on silica using ethanol as a solvent rather than water. Ho *et al.* attributed this effect to the presence of ethoxyl groups on the silica and/or Co_3O_4 surface which hindered the sintering of the particles during the thermal decomposition of nitrates. This mechanism could be at work here as we are also impregnating nitrates on silica in ethanol followed by thermal treatment. A higher dispersion would give higher catalytic activity. However, this hypothesis cannot be fully confirmed as in both cases the iron oxide particles are so small that they remain undetected even by synchrotron XRD. As for the catalyst prepared with the aqueous solution of iron precursor, no diffraction peak was observed for the catalyst prepared with the ethanolic solution of iron precursor (ESI,† Fig. S6). On the TEM images, no morphological difference was seen between these two catalysts prepared by dry impregnation either with water or with ethanol as solvent (see above, Fig. 4(b) and (c)). Finally, no real difference was noticed in the reduction temperature on the TPR profile (ESI,† Fig. S8).

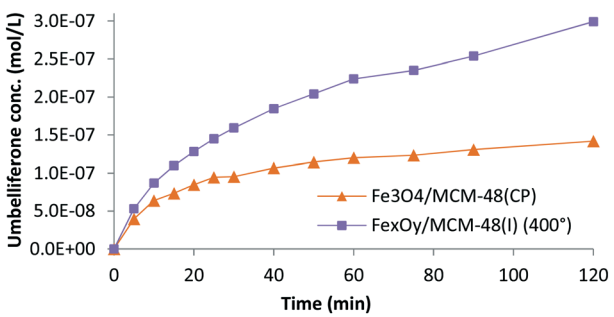

Fig. 7 Activity of the catalyst obtained by coprecipitation in the presence of the MCM-48 support and the catalyst prepared by dry impregnation and activated at 400 °C.

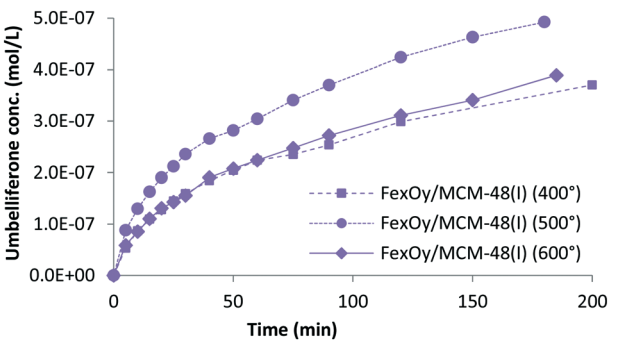

Fig. 8 Activity of the Fe_xO_y/MCM-48(I) catalyst depending on the reduction temperature.

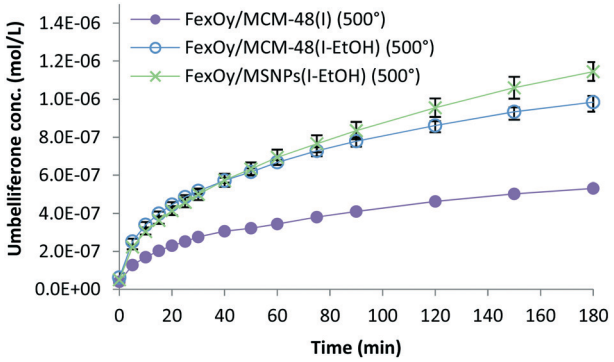

Fig. 9 Activity of the best iron oxide catalysts supported on mesoporous silica obtained by dry impregnation.

Another hypothesis that can be put forward is the influence of ethanol on surface acidity. Indeed, it has been shown that a source of protons, provided by the support, might increase HO˙ radical generation.[67] In that study, the authors however used metal organic frameworks as support and claimed the assistance of Lewis acid sites on the metal nodes.

The activity of the iron oxide catalyst supported on the MSNPs prepared by dry impregnation (Fe_xO_y/MSNPs(I-EtOH)) was slightly improved compared to that of the catalyst prepared identically but supported on MCM-48 (Fe_xO_y/MCM-48(I-EtOH)). Despite a higher specific surface area for MCM-48, these two materials have a fairly similar porosity, the difference being mainly the particle sizes (several hundred nm for the MCM-48 against only ~50 nm for the MSNPs). The difference in activity between these two catalysts can then be explained by the possibility of an intraparticular diffusion limitation. Indeed, a smaller particle size allows an easier access to the active phase located within the pores and faster exchange of reactant and departure of products with the reaction medium[68] especially in the case of short-lived species.

The initial rate of umbelliferone formation was estimated from the linear parts of the kinetic curves shown above, and the values increased by a factor of about 4.6 times (Table 3) between the less active to the most active catalysts.

Studies on the Fenton-like reaction usually investigate the degradation of organic molecules without focusing only on HO˙ radicals. The disappearance of their target molecule (which is the usual reported catalytic performance) can be due to the action of different oxidative species such as H_2O_2, HO˙, HO_2˙ or Fe^{IV}=O and not only HO˙ which makes any comparison with our results complicated.

Lin *et al.*[69] also used coumarin to measure HO˙ radical formation by their goethite catalyst. At pH 3, they estimated the initial rate of umbelliferone formation at 9×10^{-11} L mol^{-1} s^{-1}, where they used the same coumarin concentration as in our catalytic tests (1×10^{-3} mol L^{-1}). With all of our active iron oxide-based catalysts we obtained therefore a much higher initial rate of umbelliferone formation than that of Lin *et al.*, even if we used half the quantity of catalyst compared to their study (0.5 g L^{-1} and 1 g L^{-1}, respectively). Moreover, our catalytic tests are carried out near neutral pH (Milli-Q water), which is known to be less favourable than an acidic pH for Fenton chemistry.[41,42,69]

Thus, because this Fenton-like reaction is known to be more efficient at lower pH, both of these catalysts were also tested in a reaction carried out at lower pH. As expected, the reaction is more efficient as we observed a higher coumarin production (thus a higher HO˙ radical production) as shown in Fig. S14 (ESI†). The initial rate increased by a factor of 4.7 for the Fe_xO_y/MCM-48(I-EtOH) catalyst and by a factor of 5.9 for Fe_xO_y/MSNPs(I-EtOH) (Table 3). However, an important drawback with the reaction carried out in acidic medium is the leaching of iron during the reaction that increased from ppb level to ppm (ESI,† Table S1).

After catalytic tests, no XRD peak appeared, indicating that there is no formation of larger crystalline particles of Fe_xO_y compared to before the catalytic tests (ESI,† Fig. S7). Also, the XPS results (ESI,† Table S2) characterizing the catalysts after reaction show that the amount of iron at the surface of these materials decreased more when the catalytic tests were carried out at lower pH than in Milli-Q water. This

Table 3 Initial rate of umbelliferone formation depending on the catalyst

Catalyst	Initial rate of umbelliferone formation[a] (L mol^{-1} s^{-1})
Fe_3O_4/MCM-48(CP)	1.3×10^{-10}
Fe_xO_y/MCM-48(I) (400°)	1.8×10^{-10}
Fe_xO_y/MCM-48(I) (500°)	2.9×10^{-10}
Fe_xO_y/MCM-48(I) (600°)	2.0×10^{-10}
Fe_xO_y/MCM-48(I-EtOH) (500°)	6.2×10^{-10}
Fe_xO_y/MSNPs(I-EtOH) (500°)	5.9×10^{-10}
Fe_xO_y/MCM-48(I-EtOH) (500°) at pH 2.4	2.9×10^{-9}
Fe_xO_y/MSNPs(I-EtOH) (500°) at pH 2.6	3.5×10^{-9}
Plasma alone	1.2×10^{-9}
Plasma + Fe_xO_y/MCM-48(I-EtOH) (500°)	1.2×10^{-9}
Plasma + Fe_xO_y/MSNPs(I-EtOH) (500°)	1.7×10^{-9}
Plasma + Fe_xO_y/MSNPs(I-EtOH) (500°) at pH 2.8	2.7×10^{-9}

[a] The initial rate of umbelliferone formation was estimated by the slope of the curve *vs.* time at $t = 0$.

observation is in accordance with the higher iron leaching at acidic pH determined by ICP (ESI,† Table S1).

Since the most active catalysts were those obtained by dry impregnation (in EtOH as solvent), these samples were then tested for the production of HO˙ radicals under plasma exposure without adding H_2O_2, as plasma oxygen reactive species spontaneously generate H_2O_2 on contact with water.[33]

For our catalytic tests, the plasma used to generate RONS in the liquid was a cold atmospheric plasma jet operating in argon and placed a few millimeters above the surface of the liquid (thus, without direct contact with the liquid; see scheme of principle in Fig. 2).

Plasma is known to produce, among others, highly reactive oxygen species (ROS) in water including HO˙ radicals.[33] All of the highly reactive species produced by the plasma can have great potential in the medical field or for water depollution. However, in our study, we focus only on HO˙ radical detection by the selective reaction between them and coumarin (Fig. 1). This production without the presence of catalyst or H_2O_2 was measured before testing the catalytic materials. Under these 'blank' conditions, it has been possible to evaluate the production of HO˙ radicals generated in the liquid phase by the plasma alone (Fig. 10, black curve (−)). In addition, a test with MCM-48 alone exhibited no additional activity compared to the 'blank' with the plasma itself (Fig. 10, red curve (+)), indicating that mesoporous silica does not present any catalytic activity under these conditions.

The tests in the presence of iron oxide catalysts were then carried out in order to assess whether it is possible to obtain a synergistic effect between the plasma and the catalyst dispersed in the liquid phase. Indeed, with the iron oxide catalysts supported on silica, a synergy with the plasma was observed, thus producing a greater amount of HO˙ radicals than with the plasma treatment alone. However, no strong difference was observed between the two iron oxide catalysts supported on different silica nanoparticles (Fe_xO_y/MCM-48(I-EtOH) and Fe_xO_y/MSNPs(I-EtOH)) (Fig. 10, dark blue (○) and dark green (x) curves, respectively). The pH of the solution measured before treatment was ~5. After reaction, meaning after 120 minutes with plasma exposure in the presence of Fe_xO_y/MCM-48(EtOH) catalyst, the pH was 4.6. We can therefore conclude that it is not a mere effect of acidification or the reaction medium caused by the catalyst presence.

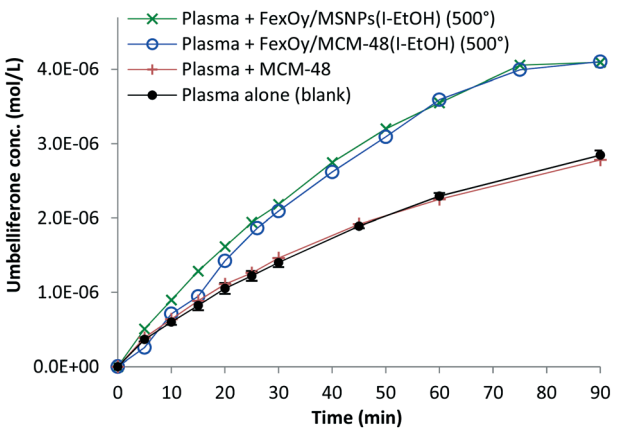

Fig. 10 Production of HO˙ radicals under plasma treatment: blank test and tests in the presence of the support alone or in the presence of iron oxide catalysts.

This synergetic effect between catalyst and plasma treatment can be explained by the presence of the neutral species H_2O_2, HO_2˙, HO˙, O_2, *etc.* In excited states that may lead to a lower activation energy barrier or additional intermediary reactions also leading to lower activation energy barriers. For example, plasma excited HO_2˙ will make the reaction of eqn (4) (see the Introduction) faster. The injection of electrons by plasma in solutions may also accelerate the regeneration of the catalyst (similarly to reaction (eqn (4))).

A reaction at lower pH with plasma treatment was also performed (ESI,† Fig. S14). A positive effect is observed, but the initial rate only increases by a factor of 1.7 when the pH is lowered to 2.8 (against a factor of 5.9 without plasma irradiation; see above). Moreover, the iron leaching becomes significant, reaching ~45 ppm (ESI,† Table S1).

To confirm the synergetic effect, we have subtracted the results of the blank (plasma alone) from the results obtained with the Fe_xO_y/MSNPs(I-EtOH) catalyst (ESI,† Fig. S15), both of these reactions being in Milli-Q water (and not at acidic pH). The obtained 'difference' curve (magenta (−)) is indeed higher than the catalytic results obtained without plasma (light green (x) curve). This confirms a synergetic effect between the solid catalyst and plasma for HO˙ radical production.

This higher production of HO˙ radicals can be explained by the sum of the radicals produced by the plasma itself and the conversion by the Fe_xO_y-based catalyst of the H_2O_2 also produced by the plasma. Indeed, it is known that during plasma–water interaction, a significant part of the HO_{aq} radicals produced by the plasma react with themselves to form H_2O_2 that then diffuses in water.[33]

Such a catalyst/plasma-enhanced behaviour has already been shown by Chandana *et al.*[57] by combining the Fenton homogeneous catalyst (iron sulfate solubilized in the reaction medium) and argon plasma jet in their study for the degradation of methylene blue. To the best of our knowledge, this is the closest result to the present work, but the added iron sulfate cannot be recovered at the end of their process, while our materials are recovered by simple filtration. Cerium-based solids were also tested in the same study, with limited efficiency. Kušić *et al.*[70] also showed an improvement in the decomposition of phenol when adding FeZSM-5 zeolite during treatment in pulsed corona reactors, which they attributed to the increase in HO˙ radicals due to the Fenton reaction between H_2O_2 and Fe^{2+} ions in the zeolite framework as well as those leached into the bulk solution. In that case, the pulsed corona reactor is a much higher energy process.

The different kinetics for umbelliferone production (logarithmic without plasma and almost linear in the presence of plasma) can be explained by the presence of

H_2O_2 in quite a large quantity since the beginning for experiments without plasma, while no H_2O_2 is present at the beginning of the experiments with plasma (H_2O_2 produced by plasma in this case). In the presence of plasma, it is also evident that the linear production rate of umbelliferone is lost after 1 h probably due to the umbelliferone and/or coumarin degradation by plasma species, but this represents only an artefact in our radical detection method, not in the catalyst/plasma activity.

Our method allowed us to obtain an aqueous phase medium enriched in HO$^{\bullet}$ radicals without consuming an external reactant, at room temperature and atmospheric pressure, thanks to a heterogeneous catalytic process based on a highly dispersed catalyst whereby the catalyst can be easily recovered by filtration. This opens the door to many applications in different fields.

Conclusions

Several techniques were used to support iron oxide nanoparticles on two different mesoporous silica supports. Either magnetite nanoparticles were synthesized separately before being supported on the silica surface, or an iron precursor was deposited by dry impregnation and reduced by thermal treatment of the solids. The optimal reduction temperature was found to be 500 °C and resulted in catalysts with ultra-small iron oxide nanoparticles inside the pores of the silica supports. All catalysts were tested for production of HO$^{\bullet}$ radicals from H_2O_2 at room temperature, neutral pH and atmospheric pressure. The materials synthesized by dry impregnation gave the best activity because a higher Fe(II) dispersion and/or a higher number of acidic sites were obtained. Moreover, the smaller particle sizes of the mesoporous silica support also allowed improvement of the catalytic performance in these experiments.

The catalysts were also used to enhance the production of hydroxyl radicals under plasma exposure. The production of HO$^{\bullet}$ radicals was significantly raised in the presence of the suspension of the Fe_xO_y-based catalysts in the aqueous phase. This has been attributed to the further transformation of H_2O_2 produced by the plasma, leading to a HO$^{\bullet}$-enriched medium that may certainly be useful for many applications like water or implant disinfection. The Fe_xO_y-based catalysts were shown to be stable even under plasma exposure and a synergetic effect between the catalyst and the plasma was highlighted.

Conflicts of interest

There are no conflicts to declare.

Acknowledgements

Financial assistance was provided within the M-Era.Net 2 transnational research program by the Belgian Fonds de la Recherche Scientifique-FNRS (F.R.S.-FNRS, Convention no. R.50.13.17.F), the National Science Centre in Poland (NCN, project no. UMO-2016/22/Z/ST8/00694) and partially by the Fonds National de la Recherche Luxembourg (FNR, project no. INTER/MERA/16/11454672). The authors also acknowledge the Spanish Government for financial support through Project PCIN-2017-128. We also thank Jean-François Statsijns for technical support, François Devred for XRD and TPR measurements, Delphine Magnin for SEM-EDX mapping and Simon Cerfontaine and Benjamin Elias for the fluorescence spectrophotometer.

References

1 E. Leyva, E. Moctezuma, K. M. Baines, S. Noriega and E. Zarazua, *Curr. Org. Chem.*, 2018, **22**, 2.
2 V. Vaiano, G. Iervolino, L. Rizzo and D. Sannino, *Curr. Org. Chem.*, 2017, **21**, 1068.
3 M. Bartolomeu, M. G. P. M. S. Neves, M. A. F. Faustino and A. Almeida, *Photochem. Photobiol. Sci.*, 2018, **17**, 1573.
4 A. Mirzaei, Z. Chen, F. Haghighat and L. Yerushalmi, *Chemosphere*, 2017, **174**, 665.
5 B. Jain, A. K. Singh, H. Kim, E. Lichtfouse and V. K. Sharma, *Environ. Chem. Lett.*, 2018, **16**, 947.
6 M. M. Bello, A. A. Abdul Raman and A. Asghar, *Process Saf. Environ. Prot.*, 2019, **126**, 119.
7 A. Dhakshinamoorthy, S. Navalon, M. Alvaro and H. Garcia, *ChemSusChem*, 2012, **5**, 46.
8 B. Palas, G. Ersöz and S. Atalay, *Ecotoxicol. Environ. Saf.*, 2019, **182**, 109367.
9 R. Gonzalez-Olmos, F. Holzer, F.-D. Kopinke and A. Georgi, *Appl. Catal., A*, 2011, **398**, 44.
10 E. G. Garrido-Ramírez, B. K. G. Theng and M. L. Mora, *Appl. Clay Sci.*, 2010, **47**, 182.
11 M. Munoz, Z. M. de Pedro, J. A. Casas and J. J. Rodriguez, *Appl. Catal., B*, 2015, **176–177**, 249.
12 X. Tang, Q. Feng, K. Liu, Z. Li and H. Wang, *J. Mater. Sci.*, 2018, **53**, 369.
13 M. C. Pereira, L. C. A. Oliveira, E. Murad and J. Adams, *Clay Miner.*, 2012, **47**, 285.
14 N. Wang, L. Zhu, D. Wang, M. Wang, Z. Lin and H. Tang, *Ultrason. Sonochem.*, 2010, **17**, 526.
15 F. Chen, S. Xie, X. Huang and X. Qiu, *J. Hazard. Mater.*, 2017, **322**, 152.
16 H. Niu, D. Zhang, S. Zhang, X. Zhang, Z. Meng and Y. Cai, *J. Hazard. Mater.*, 2011, **190**, 559.
17 N. A. Zubir, C. Yacou, J. Motuzas, X. Zhang and J. C. Diniz da Costa, *Sci. Rep.*, 2014, **4**, 4594.
18 S. S. Lin and M. D. Gurol, *Environ. Sci. Technol.*, 1998, **32**, 1417.
19 J. He, X. Yang, B. Men and D. Wang, *J. Environ. Sci.*, 2016, **39**, 97.
20 Z. Tang, Y. Liu, M. He and W. Bu, *Angew. Chem., Int. Ed.*, 2019, **58**, 946.
21 Y. Hao, Z. Dong, M. Chen, Y. Chao, Z. Liu and L. Feng, *Biomaterials*, 2020, **228**, 119568.

22 D. Xu, D. Liu, B. Wang, C. Chen, Z. Chen, D. Li, Y. Yang, H. Chen and M. G. Kong, *PLoS One*, 2015, **10**, e0128205.
23 X. Feng, H. Liu, C. He, Z. Shen and T. Wang, *Catal. Sci. Technol.*, 2018, **8**, 936.
24 E. C. Neyts, K. Ostrikov, M. K. Sunkara and A. Bogaerts, *Chem. Rev.*, 2015, **115**, 13408.
25 H. H. Kim, Y. Teramoto, A. Ogata, H. Takagi and T. Nanba, *Plasma Chem. Plasma Process.*, 2016, **36**, 45.
26 A. Nikiforov, X. Deng, Q. Xiong, U. Cvelbar, N. DeGeyter, R. Morent and C. Leys, *J. Phys. D: Appl. Phys.*, 2016, **49**, 204002.
27 D. Sun, in *Biodegradable Green Composites*, ed. S. Kalia, John Wiley & Sons, Inc., Chichester, 2016, ch. 2, pp. 18–39.
28 B. Haertel, T. von Woedtke, K. D. Weltmann and U. Lindequist, *Biomol. Ther.*, 2014, **22**, 477.
29 M. Moreau, N. Orange and M. G. J. Feuilloley, *Biotechnol. Adv.*, 2008, **26**, 610.
30 M. Keidar, A. Shashurin, O. Volotskova, M. A. Stepp, P. Srinivasan, A. Sandler and B. Trink, *Phys. Plasmas*, 2013, **20**, 057101.
31 S. Vermeylen, J. De Waele, S. Vanuytsel, J. De Backer, J. Van der Paal, M. Ramakers, K. Leyssens, E. Marcq, J. Van Audenaerde, E. L. J. Smits, S. Dewilde and A. Bogaerts, *Plasma Processes Polym.*, 2016, **13**, 1195.
32 Y. Cao, G. Qu, T. Li, N. Jiang and T. Wang, *Plasma Sci. Technol.*, 2018, **20**, 103001.
33 S. A. Norberg, W. Tian, E. Johnsen and M. J. Kushner, *J. Phys. D: Appl. Phys.*, 2014, **47**, 475203.
34 Y. Gorbanev, D. O'Connell and V. Chechik, *Chem. – Eur. J.*, 2016, **22**, 3496.
35 A. Khlyustova, C. Labay, Z. Machala, M.-P. Ginebra and C. Canal, *Front. Chem. Sci. Eng.*, 2019, **13**, 238.
36 P. J. Bruggeman, M. J. Kushner, B. R. Locke, J. G. E. Gardeniers, W. G. Graham, D. B. Graves, R. C. H. M. Hofman-Caris, D. Maric, J. P. Reid and E. Ceriani, *Plasma Sources Sci. Technol.*, 2016, **25**, 053002.
37 X. Lu, G. V. Naidis, M. Laroussi, S. Reuter, D. B. Graves and K. Ostrikov, *Phys. Rep.*, 2016, **630**, 1.
38 G. Louit, S. Foley, J. Cabillic, H. Coffigny, F. Taran, A. Valleix, J. P. Renault and S. Pin, *Radiat. Phys. Chem.*, 2005, **72**, 119.
39 H. Czili and A. Horváth, *Appl. Catal., B*, 2008, **81**, 295.
40 T. Liu and H. You, *React. Kinet., Mech. Catal.*, 2013, **109**, 233.
41 N. Wang, T. Zheng, G. Zhang and P. Wang, *J. Environ. Chem. Eng.*, 2016, **4**, 762.
42 P. V. Nidheesh, *RSC Adv.*, 2015, **5**, 40552.
43 A. V. Vorontsov, *J. Hazard. Mater.*, 2019, **372**, 103.
44 A. Rubio-Clemente, E. Chica and G. A. Peñuela, *Water, Air, Soil Pollut.*, 2015, **226**, 62.
45 K. Schumacher, M. Grün and K. K. Unger, *Microporous Mesoporous Mater.*, 1999, **27**, 201.
46 K. Möller, J. Kobler and T. Bein, *Adv. Funct. Mater.*, 2007, **17**, 605.
47 S. Natour and R. Abu-Reziq, *ChemCatChem*, 2015, **7**, 2230.
48 J. E. Lee, N. Lee, H. Kim, J. Kim, S. H. Choi, J. H. Kim, T. Kim, I. C. Song, S. P. Park, W. K. Moon and T. Hyeon, *J. Am. Chem. Soc.*, 2010, **132**, 552.
49 J. Kim, J. E. Lee, J. Lee, Y. Jang, S. W. Kim, K. An, J. H. Yu and T. Hyeon, *Angew. Chem., Int. Ed.*, 2006, **45**, 4789.
50 P. J. M. Van Espen and K. H. A. Janssens, in *Handbook of x-ray spectrometry: methods and techniques*, ed. R. E. Van Grieken and A. A. Markowicz, Marcel Dekker, Inc., New York, 1st edn, 1993, ch. 4, pp. 181–293.
51 J. Osán, J. de Hoog, P. V. Espen, I. Szalóki, C.-U. Ro and R. V. Grieken, *X-Ray Spectrom.*, 2001, **30**, 419.
52 T. Kyotani and S. Koshimizu, *Bull. Chem. Soc. Jpn.*, 2001, **74**, 723.
53 G. Boon and G. Bastin, *Microchim. Acta*, 2004, **147**, 125.
54 G. F. Bastin, J. M. Dijkstra and H. J. M. Heijligers, *X-Ray Spectrom.*, 1998, **27**, 3.
55 F. Fauth, I. Peral, C. Popescu and M. Knapp, *Powder Diffr.*, 2013, **28**, S360.
56 A. Schmidt-Bleker, S. Reuter and K.-D. Weltmann, *J. Phys. D: Appl. Phys.*, 2015, **48**, 175202.
57 L. Chandana, P. Manoj Kumar Reddy and C. Subrahmanyam, *Chem. Eng. J.*, 2015, **282**, 116.
58 S. Nigam, K. C. Barick and D. Bahadur, *J. Magn. Magn. Mater.*, 2011, **323**, 237.
59 A. Doyle and B. K. Hodnett, *Microporous Mesoporous Mater.*, 2003, **63**, 53.
60 M. Jazirehpour and S. A. S. Ebrahimi, *Ceram. Int.*, 2016, **42**, 16512.
61 M. Mashayekhi, K. Ghani, R. Shoja Razavi and N. Kiomarsipour, *J. Coat. Technol. Res.*, 2015, **12**, 1065.
62 H. Y. Lin, Y. W. Chen and C. Li, *Thermochim. Acta*, 2003, **400**, 61.
63 U. S. Khan, Amanullah, A. Manan, N. Khan, A. Mahmood and A. Rahim, *Mater. Sci.*, 2015, **33**, 278.
64 Y. H. Chen, *J. Alloys Compd.*, 2013, **553**, 194.
65 S. W. Ho and Y. S. Su, *J. Catal.*, 1997, **168**, 51.
66 Y. Zhang, Y. Liu, G. Yang, S. Sun and N. Tsubaki, *Appl. Catal., A*, 2007, **321**, 79.
67 C. Zhao, P. Dong, Z. Liu, G. Wu, S. Wang, Y. Wang and F. Liu, *RSC Adv.*, 2017, **7**, 24453.
68 E. W. Thiele, *Ind. Eng. Chem.*, 1939, **31**, 916.
69 Z. R. Lin, L. Zhao and Y. H. Dong, *Chemosphere*, 2015, **141**, 7.
70 H. Kušić, N. Koprivanac and B. R. Locke, *J. Hazard. Mater.*, 2005, **125**, 190.